

# Nematic and smectic phases with proper ferroelectric order

Grant J. Strachan,<sup>[a]\*</sup> Ewa Górecka,<sup>[a]</sup> Jadwiga Szydłowska,<sup>[a]</sup> Anna Makal,<sup>[a]</sup> Damian Pocięcha<sup>[a]</sup>

[a] Faculty of Chemistry  
University of Warsaw  
Zwirki i Wigury 101  
02-089 Warsaw, Poland  
E-mail: g.strachan@chem.uw.edu.pl

**Abstract:** A material showing a sequence of three ferroelectric liquid crystalline phases below the paraelectric nematic phase has been synthesized and studied. The polar order of molecules appearing due to the dipole-dipole interactions in the  $N_F$  phase is preserved also in the smectic phases: orthogonal  $SmA_F$  and tilted  $SmC_F$ . The ferroelectric ground state of both smectic phases was confirmed by their second harmonic generation activity and polarization switching. In  $SmC_F$  phase polarization becomes oriented to electric field by decreasing the tilt angle to zero. Although both smectic phases are ferroelectric in nature, their dielectric response was found to be very different.

Ferroelectricity is a material property that refers to the presence of spontaneous electric polarization, which is reversible on the application of an electric field. It was first discovered in Rochelle salt by J. Valasek in 1921,<sup>[1]</sup> and today, there are only around 300 known ferroelectric crystals, making it still a relatively uncommon property for crystals. Ferroelectricity is also relatively rare in soft matter. Ferroelectric polymers maintain a permanent electric polarization due to the all-*trans* conformation of polymer chains and thus parallel ordering of transverse dipole moments, and the most studied example is polyvinylidene fluoride.<sup>[2]</sup> In the 1970s, ferroelectric properties were also discovered in tilted smectic phases composed of chiral molecules.<sup>[3]</sup> In subsequent years, antiferroelectric chiral  $SmC$  phases<sup>[4]</sup> and polar properties of achiral bent-core mesogens<sup>[5]</sup> were also discovered. However, all these liquid crystals are examples of improper ferroelectrics, in which the polar order is a secondary effect. The ordering of dipole moments is induced by steric interactions between the molecules and therefore is usually weak.

For many years, it was believed that dipole-dipole interactions themselves were too weak to produce long range polar ordering in the liquid state, and the polar order would be disrupted by thermal fluctuations in the liquid. This common belief was overturned recently by the discovery of the ferroelectric nematic ( $N_F$ ) phase,<sup>[6,7]</sup> in which the spontaneous electric polarization vector is along the director. In the  $N_F$  phase the polar ordering is exceptionally strong, while the viscosity is not much different from that of regular liquids, making these materials interesting for future applications. At first glance, it seems that longitudinal polar order should be even easier to obtain in the smectic phase than in nematic phase, as thermal fluctuations in lamellar systems are strongly suppressed. The ferroelectric orthogonal smectic ( $SmA_F$ ) phase was first claimed to have been discovered in 1991,<sup>[8]</sup> but this finding turned out to be premature.<sup>[9]</sup> Since the discovery of the  $N_F$  phase, attention has also returned to the search for different ferroelectric smectic phases in combination with the polar  $N_F$  phase. This has proved challenging because the requirements for polar order and smectic order are contradictory. Smectic order generally requires molecules to have long tails to

enhance the self-segregation of mesogenic cores and alkyl chains that provides the main mechanism of layer formation. However, this inevitably increases the distance between interacting dipoles, which weakens tendency for their order. Therefore, only a limited number of mesogens that show a sequence of polar nematic and smectic phases are known so far.<sup>[10–16]</sup> In this work, we report the phase behaviour and ferroelectric properties of a new liquid crystalline material, which shows the sequence of three polar mesophases:  $N_F$ ,  $SmA_F$ , and  $SmC_F$  below the paraelectric N phase. This allows us, for the first time, to follow the development of polar order and its coupling to positional order and tilt.

The molecular structure of the material studied here is given in Figure 1, together with its phase sequence and phase transition temperatures, determined from calorimetric studies (Fig. S4). It shares the fragments with archetypal ferronematogens, RM734,<sup>[6]</sup> DIO,<sup>[7]</sup> and UUQU-4N.<sup>[17]</sup> The full synthetic and chemical characterization details are described in the SI, as well as molecular structure and crystal structure parameters obtained from single crystal X-ray diffraction (XRD) experiment (Figs S5–S7). The sequence of liquid crystalline, nematic and smectic, phases was confirmed by XRD studies. In the N and  $N_F$  phases, only short-range positional order of molecules is observed. In the  $SmA_F$  and  $SmC_F$  phases, the low-angle XRD signal narrows to become limited by instrumental broadening only, reflecting the formation of a long-range lamellar structure (Fig. 2).

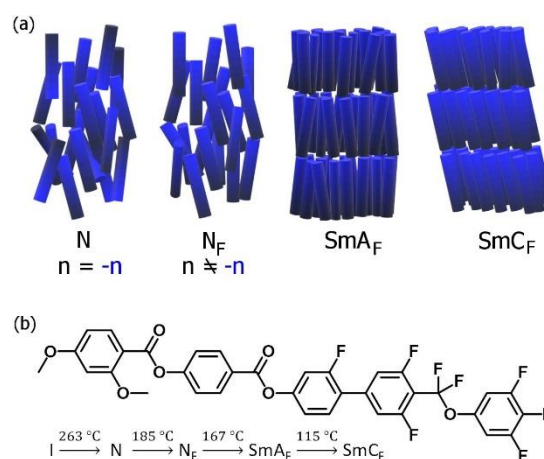


**Figure 1.** (a) Schematic drawing showing arrangement of polar molecules in N,  $N_F$ ,  $SmA_F$  and  $SmC_F$  phases. (b) The molecular structure of the mesogen reported here, with the phase transition temperatures.

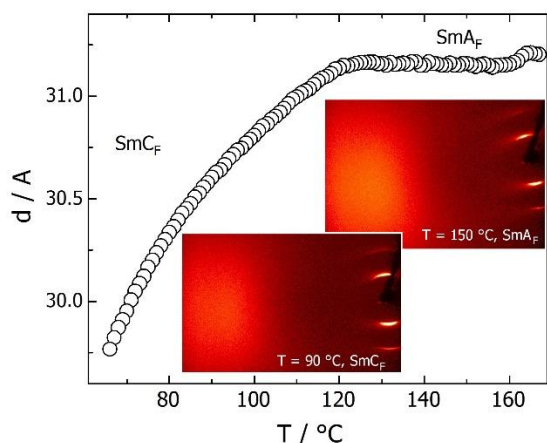


**Figure 2.** Layer spacing vs. temperature; in the inset the 2D XRD patterns registered in  $\text{SmA}_F$  and  $\text{SmC}_F$  phases, confirming liquid-like in-plane order of molecules in both phases.

In the  $\text{SmA}_F$  phase, the position of the signal corresponding to layer thickness is nearly constant and closely matches the molecular length (30 Å) determined in the crystalline state by single crystal XRD. In the  $\text{SmC}_F$  phase the layer spacing gradually decreases on lowering temperature, indicating tilting of molecules within the layers. The tilt angle estimated from the change in layer thickness a few degrees below the  $\text{SmA}_F$ - $\text{SmC}_F$  phase transition is  $\sim 15$  degrees. It should be also noted that in all LC phases the high-angle diffraction signal was diffused, consistent with a sequence of nematic and liquid-like smectic phases. The sequence of LC phases was also followed by observations of characteristic optical textures with polarized-light microscopy and measurements of optical birefringence. In thin (1.5-3  $\mu\text{m}$ ) cells with planar anchoring and parallel rubbing on both surfaces both nematic phases and the  $\text{SmA}_F$  phase gave a uniform texture, with optical axis along the rubbing direction (Fig. 3). In  $N_F$  phase several conical defects were formed anchored at the glass pillars that are cell spacers. At the transition to the  $\text{SmC}_F$  phase the uniform texture breaks into small domains, in which the optical axis departs from the rubbing direction. These domains have a characteristic blocky shape with longer sides along the rubbing direction, and they also show weak optical activity. This suggests that the molecular orientation at the lower and upper surfaces of the cell differ and inside the cell molecules twist to connect the surface layers. Interestingly, all the phases also showed birefringent textures in cells with homeotropic anchoring (Fig. S8). The schlieren texture observed in the nematic phase transformed into mosaic-like textures in polar phases, composed of clearly separated domains. The domains were smooth in  $N_F$  and  $\text{SmA}_F$  phases and broke into numerous stripes in the  $\text{SmC}_F$  phase. Optical birefringence,  $\Delta n$ , increases continuously in the nematic phase, following a critical, power-law increase of the orientational order of the molecules (Fig. 3). The trend continues also in the  $N_F$  phase, however close to the  $N$ - $N_F$  transition a pronounced dip in  $\Delta n$  is observed. Apparently, development of polar order is accompanied by strong orientational order fluctuations (splay deformation), lowering the effective optical anisotropy.

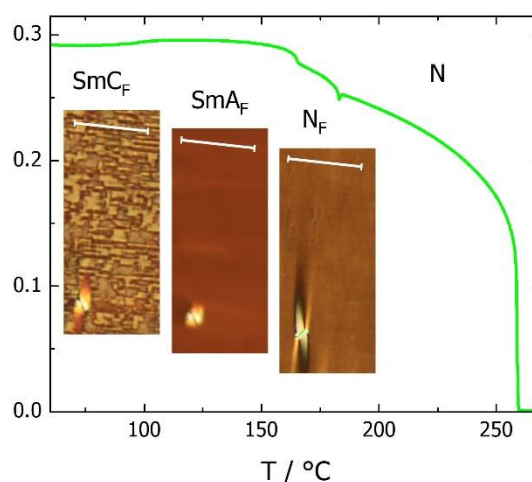


**Figure 3.** Optical birefringence,  $\Delta n$ , vs. temperature. The dip at  $N$ - $N_F$  transition reflects apparent decrease of orientational order parameter  $S$  by  $\sim 0.01$ . The step-like increase of  $\Delta n$  at  $N_F$ - $\text{SmA}_F$  phase transition correspond to  $S$  changing from 0.78 to 0.81. Inset: the optical textures of  $N_F$ ,  $\text{SmA}_F$  and  $\text{SmC}_F$  phases taken in 1.8- $\mu\text{m}$ -thick cell with planar anchoring and parallel rubbing direction on both surfaces. Scale bars correspond to 50  $\mu\text{m}$  and shows the rubbing direction, which is slightly rotated off the polarizer direction.

The  $N_F$ - $\text{SmA}_F$  phase transition is marked by a step-like increase of birefringence, indicating that the formation of long-range positional order is accompanied by a small increase in the orientational order of molecules; parameter  $S$  jumps from 0.78 to 0.81, and such a discontinuity is often observed at weakly first-order transitions. At the  $\text{SmA}_F$ - $\text{SmC}_F$  phase transition, the measured  $\Delta n$  starts to decrease, this apparent behavior may be ascribed to distortion of uniform texture as described above. Calorimetric studies revealed that three of the observed LC phases are enantiotropic, the pristine crystal melts at 145 °C to  $\text{SmA}_F$  phase, and the monotropic  $\text{SmC}_F$  phase can be observed due to the supercooling effect (Fig. S5). The  $N_F$ - $N$  phase transition was accompanied by a jump in the heat capacity, characteristic of a second-order phase transition, while at the  $\text{SmA}_F$  -  $N_F$  phase transition a small enthalpy peak was registered which is characteristic for weakly first order transitions. These findings are consistent with the optical studies. Despite the clearly seen optical texture changes at the  $\text{SmA}_F$ - $\text{SmC}_F$  phase transition, no change in the heat capacity could be seen in calorimetric measurements, suggesting that the phase transition is second order with a small change in heat capacity, below the detection limit of the DSC. The polar nature of the  $N_F$ ,  $\text{SmA}_F$ , and  $\text{SmC}_F$  phases is apparent as a clear switching current peak is registered when ac voltage is applied across the sample. The spontaneous electric polarization, calculated from the peak area, increases in the  $N_F$  phase and reaches  $\sim 5 \mu\text{C cm}^{-2}$  in smectic phases. The ferroelectric ground state of both smectic phases was confirmed by studying the switching behavior using a modified triangular wave voltage. In this experiment two successive positive voltage pulses (separated by period with zero voltage and followed by two negative ones) were applied and the switching current peak was observed only for the first pulse of each sequence (Fig. 4 and Fig. S9). Apparently, reducing the voltage from maximum value to zero preserves ferroelectric arrangement of dipoles. Moreover, all

phases below the N phase are SHG active at zero electric field, confirming their ferroelectric ground state (Fig. S10).

The application of electric field across cell thickness in  $N_F$  and  $SmA_F$  phases induces homeotropic texture as the polarization aligns along electric field (Fig. S11). In  $N_F$  phase, when the field is reduced to zero the sample relaxes immediately to birefringent state with polarization inclined to the cell surface to reduce surface bound charges.<sup>[18]</sup> In  $SmA_F$  phase the relaxation to fan texture takes place but the process is slow (takes several seconds) as the reorientation of polarization requires layer rotation. In  $SmC_F$  phase applied electric field also leads to non-birefringent state, however through an intermediate state with a pale schlieren texture (Fig. S11). Apparently in this phase weak electric field first reorients the layers but as the electric field is increased further, polarization becomes oriented to electric field by decreasing the tilt angle to zero.

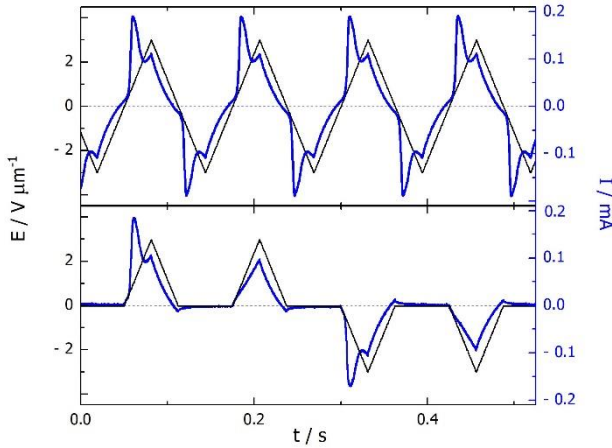


**Figure 4.** Switching current in  $SmA_F$  phase (blue lines) under application of triangular and modified triangular wave voltage (black lines). Application of two successive pulses of the same sign results in the current peak appearing only in the first pulse, confirming stable ferroelectric ground state of the phase.

Finally, dielectric spectroscopy studies were conducted. Although the interpretation of dielectric measurements for strongly polar phases is not straightforward,<sup>[19,20]</sup> and measured values of both the position and dielectric strength of relaxation modes are influenced by the thickness of the cells used, the relative changes in dielectric constant largely reflect the material properties. The studied compound was examined in 10- $\mu\text{m}$ -thick capacitor with gold electrodes and no polymer aligning layer. In the  $N_F$  phase, a strong, nearly temperature-independent dielectric response was detected, with a relaxation frequency of  $\sim 10^4$  Hz (Fig. 5). In the  $SmA_F$  phase, a much lower permittivity is measured in the whole tested frequency range,  $10^1$ - $10^7$  Hz. On lowering the temperature and upon approaching the tilted smectic phase, a weak, high frequency mode starts to build in the  $SmA_F$  phase, with a relaxation frequency that critically decreases, and a mode strength that critically increases; such a behavior is characteristic of a soft mode. In the  $SmC_F$  phase the soft mode condenses and a strong dielectric response is restored, with relaxation at  $\sim 10^4$  Hz.

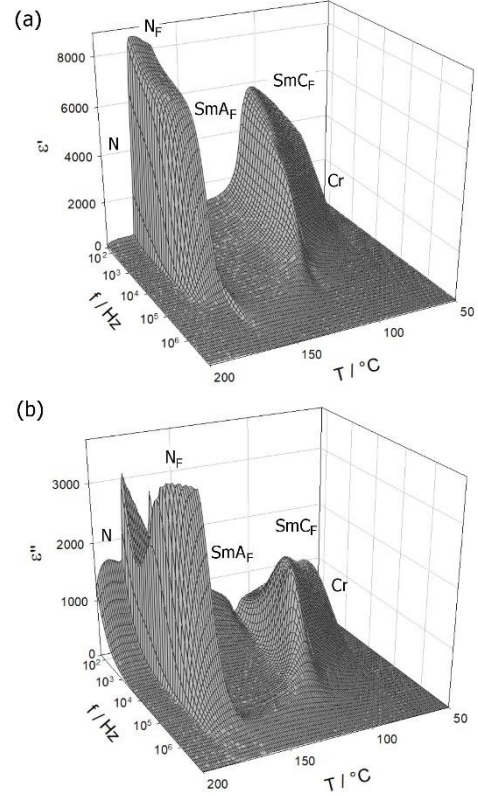


**Figure 5.** Real (a) and imaginary (b) parts of apparent dielectric permittivity measured in 10- $\mu\text{m}$ -thick cell with gold electrodes.

In summary, the material studied here shows a sequence of three ferroelectric phases:  $N_F$ - $SmA_F$ - $SmC_F$ , and our results show that the development of lamellar structure has only a minor effect on the polar order. The measured spontaneous polarization is continuous across the  $SmC_F$ ,  $SmA_F$  and  $N_F$  phases. While the  $N_F$ - $SmA_F$  phase transition is weakly first order, the  $SmA_F$ - $SmC_F$  transition is second order. Although the polarization value determined from the switching current is similar in both ferroelectric smectic phases, their dielectric response is very different. The low permittivity in the  $SmA_F$  phase in comparison to the strong response in the  $SmC_F$  phase might be explained by different types of polar fluctuations in these phases. In the non-tilted Smectic  $A_F$  phase, two basic fluctuation modes are possible: changes in the magnitude of the polarization vector and undulation of the polar layers. The first mechanism is active only when the system is 'soft', and thus can be observed only in the close vicinity of a transition to a paraelectric phase, while layer undulations in polar systems should be strongly suppressed as they produce bound charges related to local splay of the polarization vector. In the  $SmC_F$  phase, an additional fluctuation mechanism is activated due to molecular tilt – the collective rotation of molecules on the tilt cone. Due to the lower energy required for such fluctuations, the strong dielectric response is restored in this phase. Both smectic phases easily respond to electric field, in  $SmA_F$  phase under reversing electric field switching takes between the two optically homeotropic states while in  $SmC_F$  phase the schlieren texture is formed with gradually

reduced birefringence, showing that under electric field the cone angle is reduced to zero.

The new material reported here broadens the ferroelectric realm of liquid crystalline phases.

## Acknowledgements

The research was supported by the National Science Centre (Poland) under the grant no. 2021/43/B/ST5/00240.

**Keywords:** Dielectric Constant • Ferroelectric • Liquid Crystals •

- [1] J. Valasek, *Phys. Rev.* **1921**, 17, 475–481.
- [2] A. J. Lovinger, *Science* **1983**, 220, 1115–1121.
- [3] R. B. Meyer, L. Liebert, L. Strzelecki, P. Keller, *Journal de Physique Lettres* **1975**, 36, 69–71.
- [4] H. Takezoe, E. Gorecka, M. Čepič, *Rev. Mod. Phys.* **2010**, 82, 897–937.
- [5] H. Takezoe, Y. Takanishi, *Japanese Journal of Applied Physics* **2006**, 45, 597–625.
- [6] R. J. Mandle, S. J. Cowling, J. W. Goodby, *Phys. Chem. Chem. Phys.* **2017**, 19, 11429–11435.
- [7] H. Nishikawa, K. Shiroshita, H. Higuchi, Y. Okumura, Y. Haseba, S. Yamamoto, K. Sago, H. Kikuchi, *Advanced Materials* **2017**, 29, 1702354.
- [8] F. Tournilhac, L. M. Blinov, J. Simon, S. V. Yablonsky, *Nature* **1992**, 359, 621–623.
- [9] Y. Shi, F. G. Tournilhac, S. Kumar, *Phys. Rev. E* **1997**, 55, 4382–4385.
- [10] C. J. Gibb, J. Hobbs, D. I. Nikolova, T. Raistrick, S. R. Berrow, A. Mertelj, N. Osterman, N. Sebastián, H. F. Gleeson, R. J. Mandle, *Nat Commun* **2024**, 15, 5845.
- [11] J. Hobbs, C. J. Gibb, R. J. Mandle, *Small Science* **2024**, n/a, 2400189.
- [12] Y. Song, M. Deng, Z. Wang, J. Li, H. Lei, Z. Wan, R. Xia, S. Aya, M. Huang, *J. Phys. Chem. Lett.* **2022**, 13, 9983–9990.
- [13] H. Kikuchi, H. Matsukizono, K. Iwamatsu, S. Endo, S. Anan, Y. Okumura, *Advanced Science* **2022**, 9, 2202048.
- [14] H. Matsukizono, K. Iwamatsu, S. Endo, Y. Okumura, S. Anan, H. Kikuchi, *J. Mater. Chem. C* **2023**, 11, 6183–6190.
- [15] J. Karcz, J. Herman, N. Rychłowiec, P. Kula, E. Górecka, J. Szydłowska, P. W. Majewski, D. Pocięcha, *Science* **2024**, 384, 1096–1099.
- [16] H. Nishikawa, D. Okada, D. Kwaria, A. Nihonyanagi, M. Kuwayama, M. Hoshino, F. Araoka, *Advanced Science* **n.d.**, n/a, 2405718.
- [17] A. Manabe, M. Bremer, M. Kraska, *Liquid Crystals* **2021**, 48, 1079–1086.
- [18] P. Kumari, B. Basnet, H. Wang, O. D. Lavrentovich, *Nat Commun* **2023**, 14, 748.
- [19] N. A. Clark, X. Chen, J. E. MacLennan, M. A. Glaser, *Phys. Rev. Res.* **2024**, 6, 013195.
- [20] V. Matko, E. Gorecka, D. Pocięcha, J. Matraszek, N. Vaupotič, **2024**, DOI 10.48550/arXiv.2401.16084.

## Nematic and smectic phases with proper ferroelectric order

Grant J. Strachan, Ewa Górecka, Jadwiga Szydłowska, Anna Makal, Damian Pocięcha

Experimental methods .....	5
Synthetic procedures and chemical characterisation .....	6
Single crystal X-ray diffraction .....	9
Supplementary figures.....	14
Supplemental references .....	16

### Experimental Methods

Transition temperatures and the associated enthalpy changes were measured by differential scanning calorimetry using a TA DSC Q200 instrument. Measurements were performed under a nitrogen atmosphere with a heating/cooling rate of 10 K min<sup>-1</sup>, unless otherwise specified.

Observations of optical textures of liquid crystalline phases was carried out by polarised-light optical microscopy using a Zeiss AxioImager.A2m microscope equipped with a Linkam heating stage.

Optical birefringence was measured with a setup based on a photoelastic modulator (PEM-90, Hinds) working at a modulation frequency  $f = 50$  kHz; as a light source a halogen lamp (Hamamatsu LC8) equipped with narrow bandpass filters was used. The transmitted light intensity was monitored with a photodiode (FLC Electronics PIN-20) and the signal was deconvoluted with a lock-in amplifier (EG&G 7265) into  $1f$  and  $2f$  components to yield a retardation induced by the sample. Knowing the sample thickness, the retardation was recalculated into optical birefringence. Samples were prepared in 1.6- $\mu$ m-thick cells with planar anchoring. The alignment quality was checked prior to measurement by inspection under the polarised-light optical microscope.

X-ray diffraction measurements of samples in liquid crystalline phases were carried out using a Bruker D8 GADDS system, equipped with micro-focus-type X-ray source with Cu anode and dedicated optics and VANTEC2000 area detector. Small angle diffraction experiments were performed on a Bruker Nanostar system ( $\mu$ S microfocus source with copper target, MRI heating stage, Vantec 2000 area detector).

Single-crystal X-ray diffraction data were collected on a SuperNova diffractometer with micro-focus sealed source of MoK $\alpha$  X-ray radiation ( $\lambda = 0.71073$  Å) and CCD Eos detector. Single crystals of studied compound were obtained from a chloroform solution using hexane as an antisolvent. A suitable crystal – a colorless prism - was mounted on a nylon loop with a trace of ParatoneN oil. The crystal was kept at 120.00(10) K during data collection in cold nitrogen stream using Oxford Cryosystems device. Data reduction was performed with CrysAlisPro.<sup>[21]</sup> Gaussian absorption correction was applied using spherical harmonics with SCALE3 ABSPACK algorithm. Using Olex2,<sup>[22]</sup> the structure was solved with the olex2.solve<sup>[23]</sup> program using Charge Flipping and refined with the olex2.refine<sup>[23]</sup> package using Gauss-Newton minimization. H-atom positions were identifiable from a difference Fourier map but were refined with distances restrained to standardized values and the atomic displacement parameters (ADP-s) of H atoms were restrained as ‘riding’ on the displacement parameters of the covalently bound non-H atoms. A static disorder concerning the position of the fluorine F8 was refined, yielding 93% of the major component (F8 bound to C19) and 7% of the minor component with F8a bound to C15. Similarity restraints were applied for C – F distances and F displacement parameters of both disorder components.

Spontaneous electric polarisation was determined by integration of the current peaks recorded during polarization switching upon applying a triangular-wave voltage. A 5- $\mu$ m-thick cells with ITO or gold electrodes and no polymer aligning layers were used, and the switching current was determined by recording the voltage drop on a resistor connected in series with the sample.

The SHG response was investigated using a microscopic setup based on a solid-state laser EKSPLA NL202. Laser pulses (9 ns) at a 10 Hz repetition rate and max. 2 mJ pulse energy at  $\lambda=1064$  nm were applied. The pulse energy was adjusted for each sample to avoid its decomposition. The infra-red beam was incident onto a LC homogenous

## Supporting Information

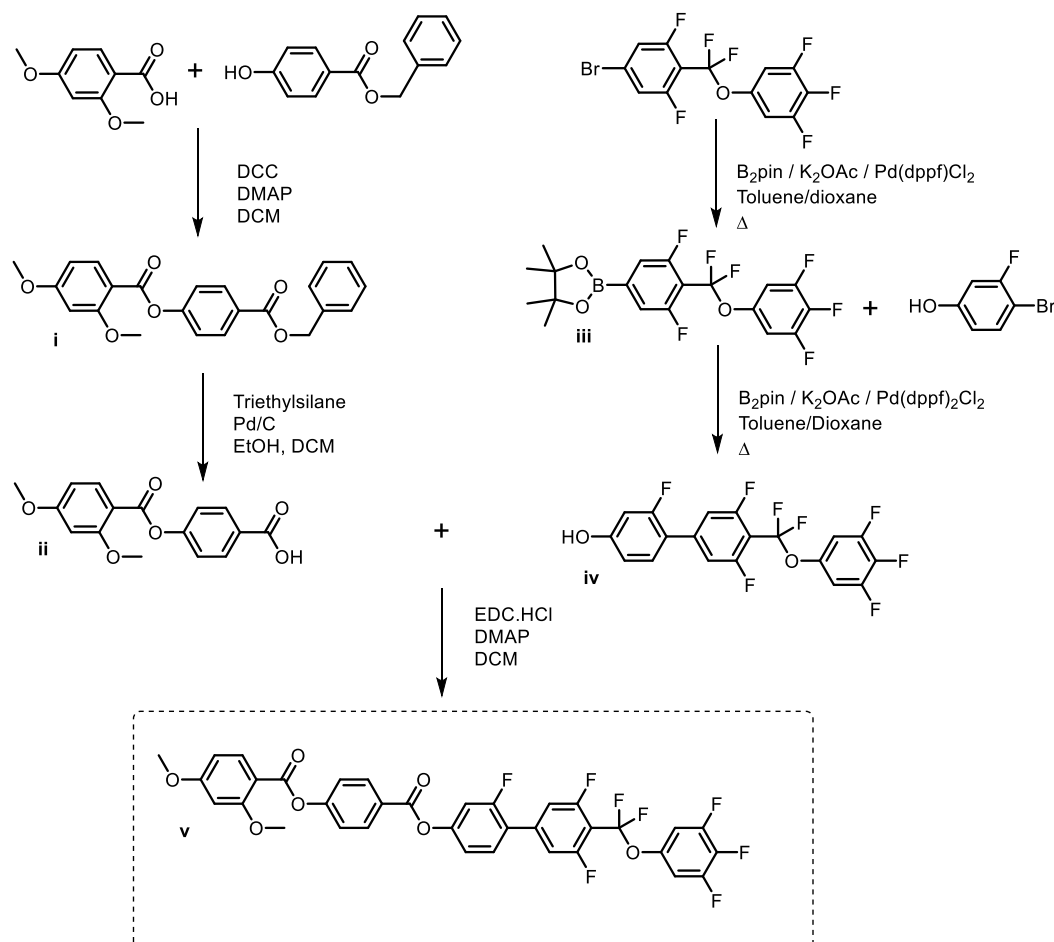
cell of thickness 5  $\mu\text{m}$ . An IR pass filter was placed at the entrance to the sample and a green pass filter at the exit of the sample.

The complex dielectric permittivity,  $\epsilon^*$ , was measured using a Solartron 1260 impedance analyser, in the 1 Hz – 10 MHz frequency range, and a probe voltage of 50 mV. The material was placed in a 5- or 10- $\mu\text{m}$ -thick glass cell with gold electrodes. Cells without polymer aligning layers were used, as the presence of the thin (~10 nm) polyimide layers at the cell surfaces acts as an additional high capacitance capacitor in a series circuit with the capacitor filled with the LC sample, which for materials with very high values of permittivity, may strongly affect the measured permittivity of the LC phases. Lack of a surfactant layer resulted in a random configuration of the director in the LC phases.

## Synthetic Procedures and Structural Characterisation

Unless otherwise stated, all materials were obtained from commercial sources and used without further purification. Reactions were monitored using thin layer chromatography (TLC) using aluminium-backed plates with a coating of Merck Kieselgel 60 F254 silica and an appropriate solvent system. Spots were visualised using UV light (254 nm). Flash column chromatography was carried out using silica grade 60 Å 40-63 micron.

FT-IR spectra were obtained using a Nicolet iS50 FT-IR spectrometer.  $^1\text{H}$  and  $^{13}\text{C}$  NMR spectra were recorded on a 400 MHz Agilent NMR spectrometer using either  $\text{CDCl}_3$  or  $\text{DMSO}-d_6$  as solvent and using residual non-deuterated trace solvents as reference. Chemical shifts ( $\delta$ ) are given in ppm relative to TMS ( $\delta = 0.00$  ppm). Mass spectroscopy was conducted on a Micromass LCT instrument.



Scheme 1: Synthetic route to the new material reported here.

Compounds **i**,<sup>[24]</sup> **ii**,<sup>[24]</sup> **iii**,<sup>[25]</sup> and **iv**<sup>[15]</sup> have been previously reported.

### Benzyl ester **i**

2,4-dimethoxy benzoic acid (1.190 g, 6.6 mmol, 1.1 eq) and *N,N'*-dicyclohexylcarbodiimide (DCC) (1.730 g, 8.4 mmol, 1.4 eq) were dissolved in DCM (50 ml) and stirred for 10 minutes. Benzyl 4-hydroxybenzoate (1.371 g, 6 mmol, 1 eq) and 4-dimethylaminopyridine (DMAP) (74 mg, 0.6 mmol, 0.1 eq) were added and the reaction was left

## Supporting Information

stirring at room temperature overnight. The reaction was filtered to remove the dicyclohexylurea and the solvent removed *in vacuo*. The crude product was recrystallised from ethanol to yield the product as a white solid. (1.27 g, 54 %).

$^1\text{H}$  NMR (400 MHz,  $\text{CDCl}_3$ )  $\delta$  8.13 (d,  $J = 8.6$  Hz, 2H), 8.07 (d,  $J = 8.7$  Hz, 1H), 7.39 (overlapping multiplets, 5H), 7.28 (d,  $J = 8.6$  Hz, 2H), 6.56 (dd,  $J = 8.7, 2.2$  Hz, 1H), 6.53 (d,  $J = 2.2$  Hz, 1H), 5.37 (s, 2H), 3.91 (s, 3H), 3.89 (s, 3H).  $^{13}\text{C}$  NMR (101 MHz,  $\text{CDCl}_3$ )  $\delta$  165.81, 165.20, 162.95, 162.39, 154.97, 135.99, 134.58, 131.17 (2C), 128.60 (2C), 128.25, 128.17 (2C), 127.25, 122.02 (2C), 110.61, 104.86, 98.98, 66.74, 56.02, 55.60.

### Acid ii

Under an argon atmosphere triethylsilane (1.6 ml, 10 mmol, 10 eq.) was added dropwise to a stirred solution of **i** (393 mg, 1 mmol) and 5 % Pd/C (80 mg) in ethanol (3 ml) and DCM (3 ml). The reaction was stirred for 5 minutes after addition was complete, then filtered through celite and the solvent removed *in vacuo*. The crude product was washed with hexane to yield the product as a white powder. (300 mg, quant.)  $R_f$  0.22 (DCM)

$^1\text{H}$  NMR (400 MHz,  $\text{CDCl}_3$ )  $\delta$  8.15 (d,  $J = 8.5$  Hz, 2H), 8.08 (d,  $J = 8.8$  Hz, 1H), 7.32 (d,  $J = 8.5$  Hz, 2H), 6.57 (dd,  $J = 8.8, 2.2$  Hz, 1H), 6.54 (d,  $J = 2.2$  Hz, 1H), 3.93 (s, 3H), 3.90 (s, 3H).  $^{13}\text{C}$  NMR (101 MHz,  $\text{DMSO}-d_6$ )  $\delta$  167.16, 165.35, 163.00, 162.15, 154.67, 134.44, 131.27 (2C), 128.70, 122.70 (2C), 110.32, 106.14, 99.43, 56.43, 56.16.

### Boronic ester iii

A solution of 5-bromo-2-(difluoro(3,4,5-trifluorophenoxy)methyl)-1,3-difluorobenzene (4.951 g 12.7 mmol), bis(pinacolato)diboron (3.35 g 12.7 mmol), anhydrous potassium acetate (3.67 g 36.7 mmol) in toluene (100 ml) and 1,4-dioxane (100 ml) was sparged with argon for 1 hr. Then the catalyst Pd(dppf) $\text{Cl}_2$  (280 mg, 3 mol%) was added and the reaction was stirred at 80°C for 5 hrs. The reaction was cooled to room temperature and added to 1M HCl solution. The product was extracted with toluene and the organic layer was washed three times with water and dried over  $\text{MgSO}_4$ . The solvent was removed under vacuum and the crude solid thus obtained was recrystallized from ethanol. Yield 2.5 g, 45 %).

$^1\text{H}$  NMR (400 MHz,  $\text{CDCl}_3$ )  $\delta$  7.38 (d,  $J = 10.5$  Hz, 2H), 6.96 (m, 2H), 1.35 (s, 12H).  $^{13}\text{C}$  NMR (101 MHz,  $\text{CDCl}_3$ )  $\delta$  160.81, 160.78, 160.78, 158.23, 158.20, 152.26, 152.26, 152.20, 152.15, 152.15, 152.10, 149.76, 149.76, 149.71, 149.65, 149.65, 149.60, 144.72, 144.61, 144.58, 144.52, 144.47, 139.79, 139.63, 139.63, 139.48, 137.29, 137.14, 136.99, 122.83, 120.18, 120.18, 118.17, 118.14, 118.12, 118.12, 117.96, 117.95, 117.92, 117.92, 111.65, 111.42, 111.19, 107.52, 107.45, 107.35, 107.28, 84.86, 77.30, 76.99, 76.67, 24.80.

### Phenol iv

Intermediate **iii**, (1.108 g, 2.5 mmol) 4-bromo-3-fluorophenol, (0.587 g, 2.7 mmol) and potassium phosphate trihydrate (2.32 g, 8.7 mmol) were dissolved in THF (20 ml) and distilled water (1 ml), sparged with argon, and refluxed for 1 hour. Palladium acetate (33 mg, 0.15 mmol) and S-Phos (101 mg, 0.25 mmol) were added, and the reaction was refluxed for 4 hours. The mixture was cooled to RT, acidified with 1 M HCl, extracted with three portions of DCM and the organic layers were combined, dried over magnesium sulfate and the solvent removed *in vacuo*. The crude product was recrystallised from hexane to yield the desired product. (404 mg, 38 %).

$^1\text{H}$  NMR (400 MHz,  $\text{CDCl}_3$ )  $\delta$  7.31 (t,  $J = 8.6$  Hz, 1H), 7.16 (d,  $J = 11.0$  Hz, 2H), 6.99 (m, 2H), 6.72 (m, 2H), 5.39 (s, 1H).  $^{13}\text{C}$  NMR (101 MHz,  $\text{CDCl}_3$ )  $\delta$  161.55, 161.16, 161.10, 159.05, 158.62, 158.60, 158.54, 157.86, 157.74, 152.28, 152.23, 152.17, 152.12, 149.79, 149.74, 149.68, 149.63, 141.51, 141.40, 141.30, 139.80, 139.65, 139.50, 137.31, 137.16, 137.00, 130.84, 130.79, 120.22, 118.06, 117.94, 112.76, 112.73, 112.70, 112.52, 112.49, 112.45, 112.16, 112.13, 107.55, 107.48, 107.37, 107.31, 104.21, 103.96.  $^{19}\text{F}$  NMR (376 MHz,  $\text{CDCl}_3$ )  $\delta$  -61.72 (t,  $J = 26.3$  Hz, 2F), -111.03 (td,  $J = 26.3, 10.3$  Hz, 2F), -114.51 (t,  $J = 10.3$  Hz, 1F), -132.53 (dd,  $J = 20.9, 8.0$  Hz, 2F), -163.22 (tt,  $J = 20.9, 5.8$  Hz, 1F).

### Target ester v

Intermediate acid **iii** (71 mg, 0.24 mmol) and EDC.HCl (62 mg, 0.32 mmol) were dissolved in 10 ml DCM and stirred for 5 minutes. Phenol **iv** (90 mg, 0.21 mmol) and DMAP (3 mg, 0.02 mmol) were added, and the mixture stirred overnight and monitored by TLC ( $R_f$  0.58 DCM). The reaction mixture was washed 3 times with water and the organic layer dried over magnesium sulfate and removed *in vacuo*. The crude solid was purified by column chromatography (gradient elution, 50/50 DCM: hexane  $\rightarrow$  DCM) and triturated with hexane. Yield 63 mg (42 %).

$^1\text{H}$  NMR (400 MHz,  $\text{CDCl}_3$ )  $\delta$  8.26 (d,  $J = 8.6$  Hz, 2H), 8.10 (d,  $J = 8.7$  Hz, 1H), 7.50 (t,  $J = 8.5$  Hz, 1H), 7.39 (d,  $J = 8.5$  Hz, 2H), 7.27 – 7.14 (overlapping multiplets and chloroform, 5H), 7.04 – 6.97 (m, 2H), 6.58 (d,  $J = 9.1$  Hz, 1H), 6.55 (s, 1H), 3.94 (s, 3H), 3.91 (s, 3H).  $^{13}\text{C}$  NMR (101 MHz,  $\text{CDCl}_3$ )  $\delta$  165.35, 163.97, 162.80, 162.50, 161.22, 161.16, 160.78, 158.65, 158.59, 158.27, 155.83, 152.39, 152.30, 152.28, 152.25, 152.20, 152.15, 149.81, 149.76, 149.70, 149.65, 140.90, 140.87, 140.77, 140.77, 140.67, 140.64, 139.84, 139.71, 139.69, 139.54, 137.35, 137.20, 137.05, 134.63, 131.82, 130.56, 130.52, 125.77, 123.28, 123.25, 123.13, 122.44, 120.11, 120.08, 118.50, 118.47, 113.24, 113.21, 113.18, 113.00, 112.97, 112.93, 111.07, 110.81, 110.35, 107.58, 107.52, 107.41, 107.34, 104.94, 98.98, 56.04, 55.62.  $^{19}\text{F}$  NMR (376 MHz,  $\text{CDCl}_3$ )  $\delta$  -61.82 (t,  $J = 26.4$  Hz, 2F), -110.45 (td,  $J = 26.4, 10.4$  Hz, 2F), -113.83 – -113.93 (m, 1F), -132.37 – -132.55 (m, 2F), -163.12 (tt,  $J = 20.9, 5.9$  Hz, 1F).

HRMS (ESI)  $m/z$  Calculated for  $\text{C}_{35}\text{H}_{20}\text{O}_7\text{F}_8$ :

## Supporting Information

[M+H]<sup>+</sup> theoretical mass: 705.11540, found 705.11657, difference 1.65 ppm.

[M+Na]<sup>+</sup> theoretical mass: 727.09735, found 727.09838, difference 1.42 ppm.

IR ( $\nu_{\max}/\text{cm}^{-1}$ ) 3101, 3074, 3005, 2926, 2847, 1741, 1710, 1611, 1519, 1233, 1135, 1037.

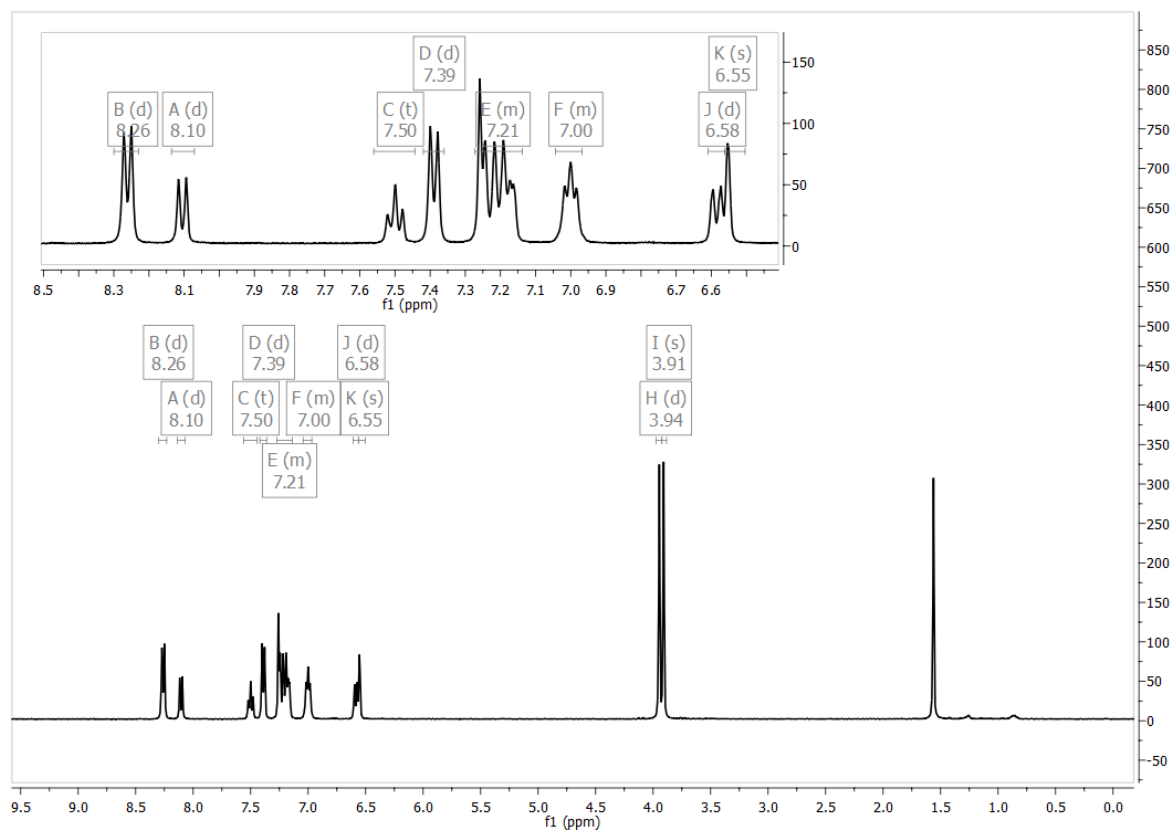


Figure S1: <sup>1</sup>H NMR spectrum of compound **v** in CDCl<sub>3</sub>.

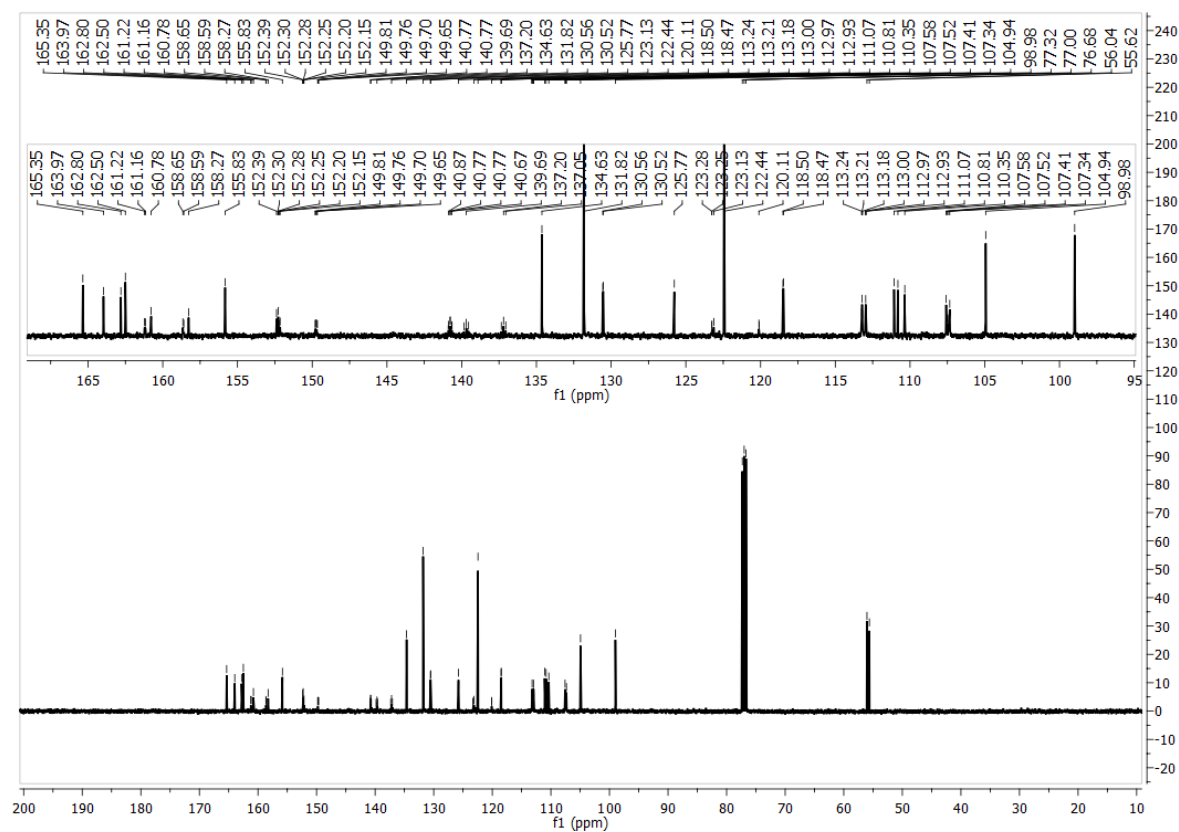


Figure S2: <sup>13</sup>C NMR spectrum of compound **v** in CDCl<sub>3</sub>.



## Supporting Information

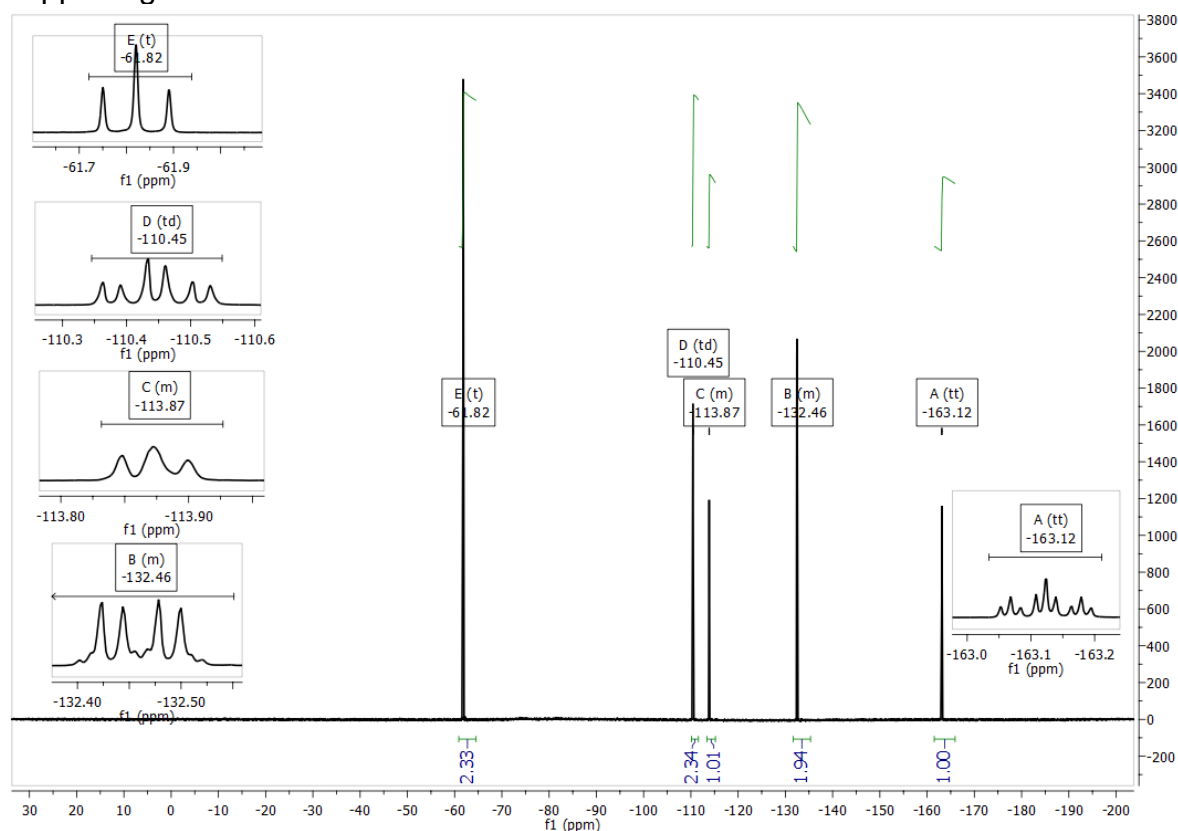


Figure S3:  $^{19}\text{F}$  NMR spectrum of compound **v** in  $\text{CDCl}_3$ .

## Single crystal X-ray diffraction

The material crystallized in centrosymmetric P-1 space group in triclinic system, with one independent molecule in the asymmetric unit. There were no traces of the solvent molecules in voids in this crystal structure. There is a static disorder concerning the position of the fluorine F8 with 93% of the major component with F8 bound to C19 and 7% of the minor component (F8a bound to C15, Figure S4).

The molecule in the crystal structure is fully stretched with no co-planar phenyl rings. The terminal rings #1 and #5 are nearly perpendicular to the closest-connected rings #2 and #4 accordingly, while the three middle rings are rotated at about  $40^\circ$  with respect to each other (Fig. S4 and Table S1), in order to avoid short F ... F and F ... H intramolecular contacts. The ester groups are also not co-planar with the attached phenyl rings: O2 and O4 atoms are out of plane of the ring #4 and #5 accordingly by  $24.83(17)^\circ$  and  $23.45(17)^\circ$ .

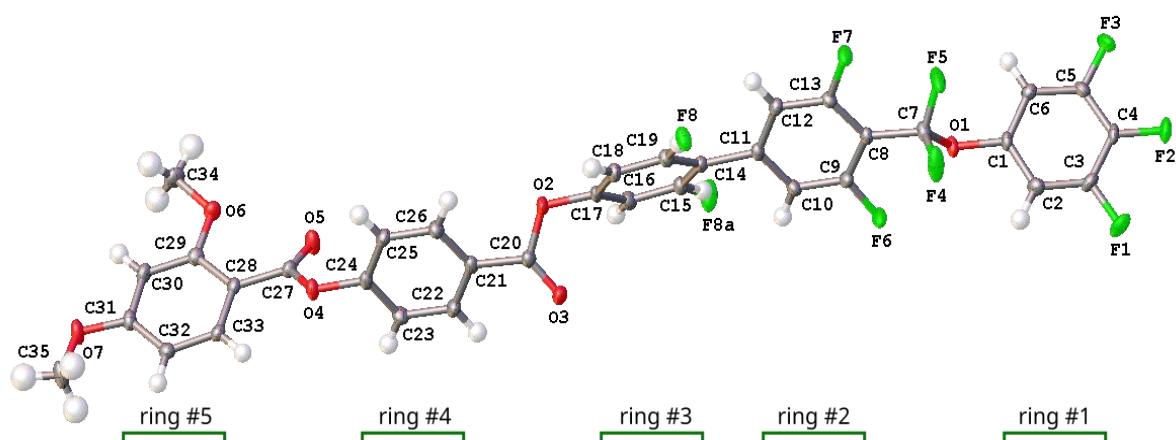


Figure S4. Determined structure of molecule with the applied numbering scheme. H atom numbers are the same as those of the closest covalently bound C atom. Atomic displacement parameters represented at 50% probability level. The minor variant of disorder labelled as F8a. Aromatic rings in the structure have been assigned numbers based on the order of C atoms.

## Supporting Information

Table S1. Angles between the planes of the phenyl rings.

Phenyl rings	Angle [°]
#1 - #2	126.81(6)
#2 - #3	39.91(6)
#3 - #4	36.53(6)
#4 - #5	107.36(6)

The most important intermolecular interactions have been identified using interaction energy estimation with UNI potential<sup>[26,27]</sup> within Mercury<sup>[28]</sup> and illustrated in Figure S5. Notably, the two strongest interactions involve intermolecular  $\pi \dots \pi$  stacking of the ring #5 with its symmetry-related equivalent and #2 with #4, while the third occurs between the molecules related by translation and appears to arise from maximizing the number of C – H ... F interactions (Tables S2, S3).

As a consequence, the molecules all align approximately with the crystallographic [1-1-1] direction but do not form separate columns or layers in the crystal structure (Figure S7).

Table S2. Geometry of intermolecular  $\pi \dots \pi$  interactions in the crystal structure.

phenyl rings involved	inter-planar angle [°]	inter-centroid distance [Å]	lateral shift [Å]
#1---#1(-1+X,1+Y,+Z)	3.422(6)	3.877(6)	1.773(6)
#2---#4(-X,1-Y,1-Z)	0.000	3.745(7)	1.786(7)
#5---#5(4-X,-2-Y,-Z)	0.000	3.514(6)	1.102(7)

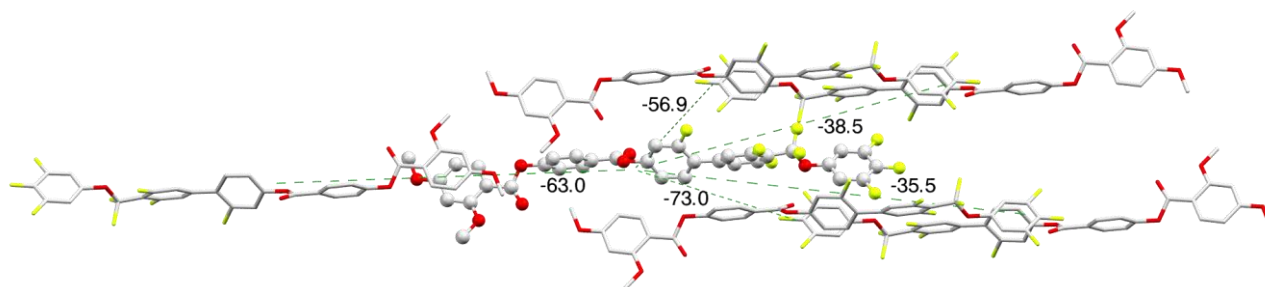


Figure S5. The most important intermolecular interactions in the crystal structure represented as dashed lines between the centers of interacting molecules. Among the three strongest interactions, two rely on  $\pi \dots \pi$  stacking.

## Supporting Information

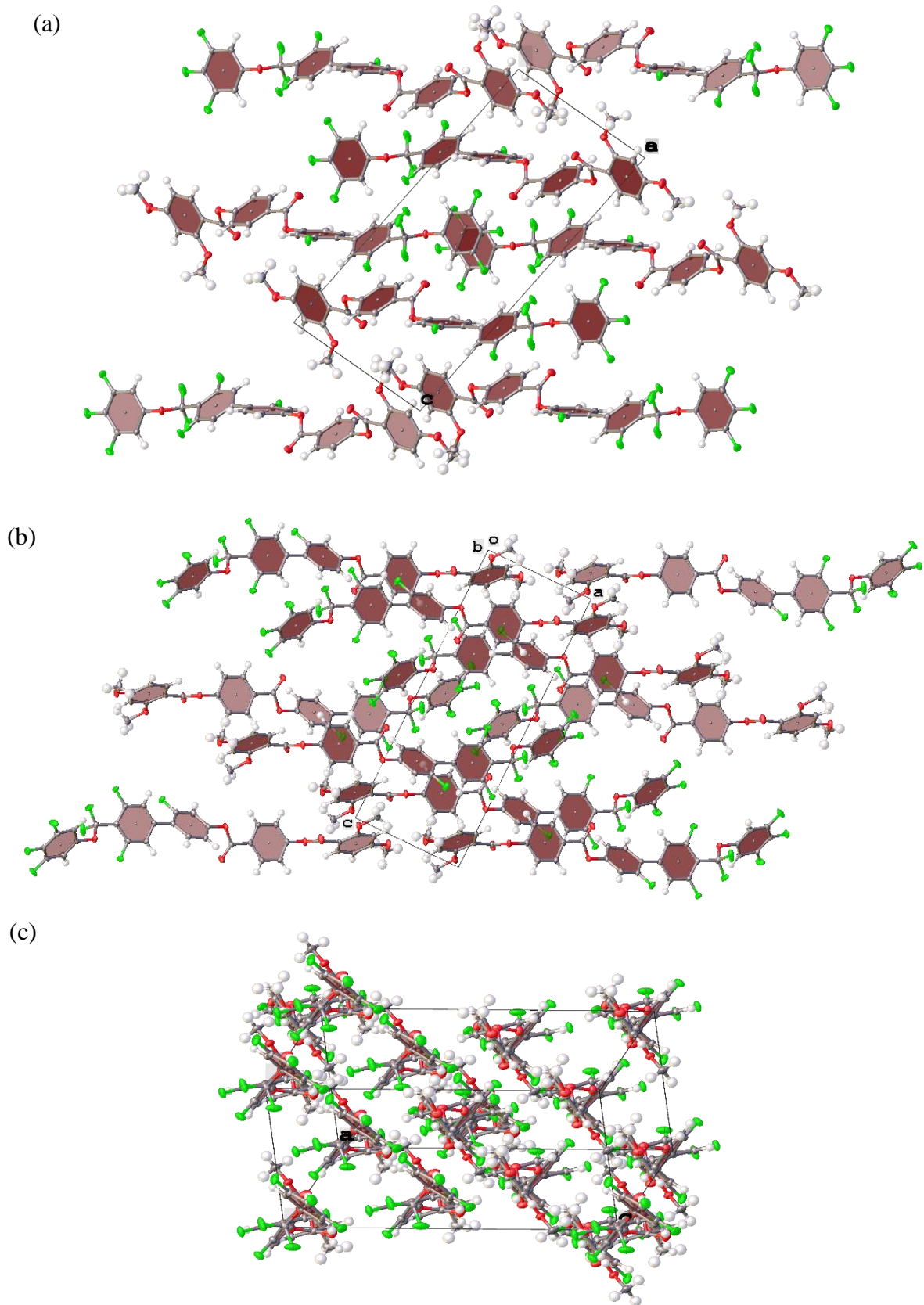


Figure S6. Visualization of crystal packing in selected directions: (a) view along  $[100]$ , (b) view along  $[010]$  and (c) view along  $[1-1-1]$ . Phenyl rings outlined in brown.

## Supporting Information

Table S3. The strongest intermolecular interactions.

	Intermolecular Distance [Å]	Energy [ kJ/mol]	
1	11.16	-72.9	$\pi \dots \pi$ interactions (ring #5)
2	20.83	-63.0	$\pi \dots \pi$ interactions (rings #2 and #4)
3	7.82	-56.8	C – H ... F and C – H ... $\pi$
4	19.78	-38.5	C – H ... F and C – H ... $\pi$
5	24.16	-35.5	$\pi \dots \pi$ interactions (ring #1)

The final crystal structure was deposited with the CCDC (**CCDC Number 2375621**).

Detailed information on X-ray data and crystal structure model were summarized in Table S4.

Table S4. Crystal data and structure refinement for the studied compound

Empirical formula	C <sub>35</sub> H <sub>20</sub> F <sub>8</sub> O <sub>7</sub>
CCDC code	2375621
Formula weight	704.532
Temperature/K	120.00(10)
Crystal system	triclinic
Space group	P-1
a/Å	7.8233(3)
b/Å	9.3769(4)
c/Å	20.2777(8)
$\alpha$ /°	83.455(3)
$\beta$ /°	89.797(3)
$\gamma$ /°	80.365(3)
Volume/Å <sup>3</sup>	1456.82(10)
Z	2
$\rho$ calc/cm <sup>3</sup>	1.606
$\mu$ /mm <sup>-1</sup>	0.145
F(000)	716.7
Crystal size/mm <sup>3</sup>	0.211 × 0.098 × 0.037
Radiation	Mo K $\alpha$ ( $\lambda$ = 0.71073)
2 $\theta$ range for data collection/°	4.04 to 58.9
Index ranges	-10 ≤ h ≤ 10, -12 ≤ k ≤ 12, -26 ≤ l ≤ 27
Reflections collected	21214
Independent reflections	7454 [R <sub>int</sub> = 0.0426, R <sub>sigma</sub> = 0.0477]
Data/restraints/parameters	7454/1/463
Goodness-of-fit on F <sup>2</sup>	1.056
Final R indexes [ $I \geq 2\sigma(I)$ ]	R <sub>1</sub> = 0.0517, wR <sub>2</sub> = 0.1078
Final R indexes [all data]	R <sub>1</sub> = 0.0700, wR <sub>2</sub> = 0.1165
Largest diff. peak/hole / e Å <sup>-3</sup>	0.46/-0.34

## Supporting Information

Intermolecular energy estimation was based on an empiric potential,<sup>[26,27]</sup>  
Potential =  $A \cdot \exp(-Br) - Cr(-6)$

with unified parameters according to Table S5.

Table S5. Unified (UNI) pair-potential parameters:

atom1	atom2	A	B	C
F7	F7	170916.4	4.22	564.8
F7	O4	182706.1	3.98	868.3
F7	O5	182706.1	3.98	868.3
F7	C31	196600.9	3.84	1168.8
F7	H10	64257.8	4.11	248.4
O4	O4	195309.1	3.74	1335.0
O4	O5	195309.1	3.74	1335.0
O4	C31	393086.8	3.74	2682.0
O4	H10	295432.3	4.82	439.3
O5	O5	195309.1	3.74	1335.0
O5	C31	393086.8	3.74	2682.0
O5	H10	295432.3	4.82	439.3
C31	C31	226145.2	3.47	2418.0
C31	H10	120792.1	4.10	472.8
H10	H10	24158.0	4.01	109.2

## Supplementary figures

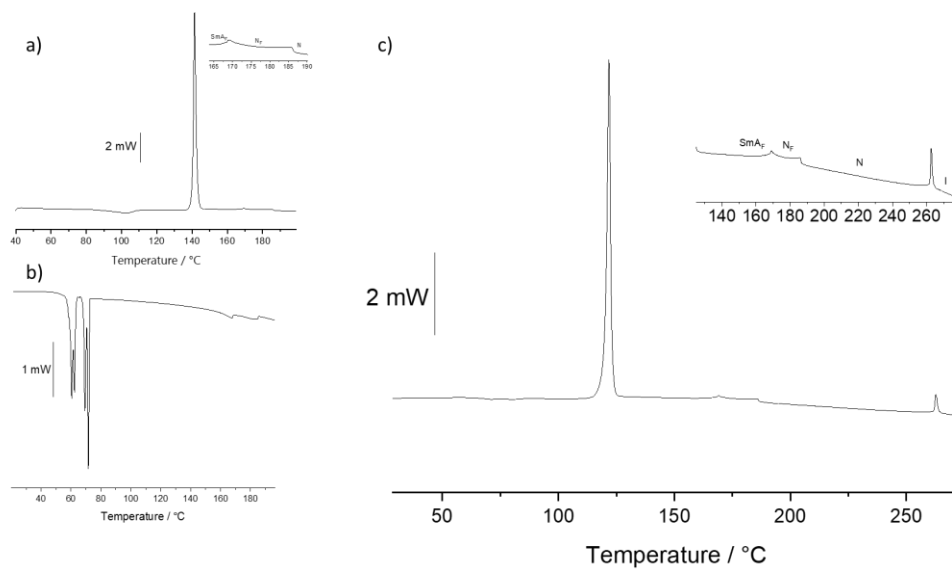


Figure S7: DSC traces for the new material reported here: a) first heating cycle, to avoid decomposition the temperature range was limited to 180 °C b) cooling cycle, c) second heating cycle.

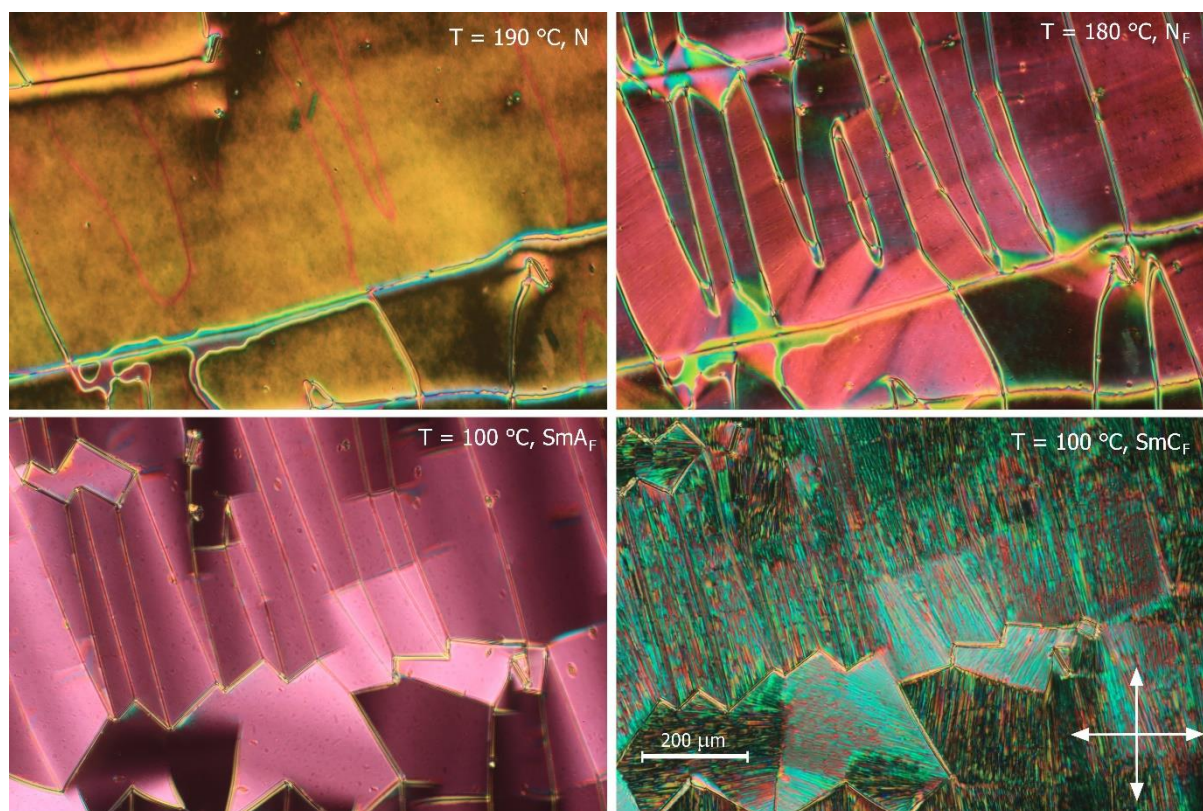


Figure S8: Optical textures observed with polarized light microscope in LC phases of reported compound, in 5- $\mu$ m-thick cell with homeotropic anchoring. Arrows indicate polarizers direction.

## Supporting Information

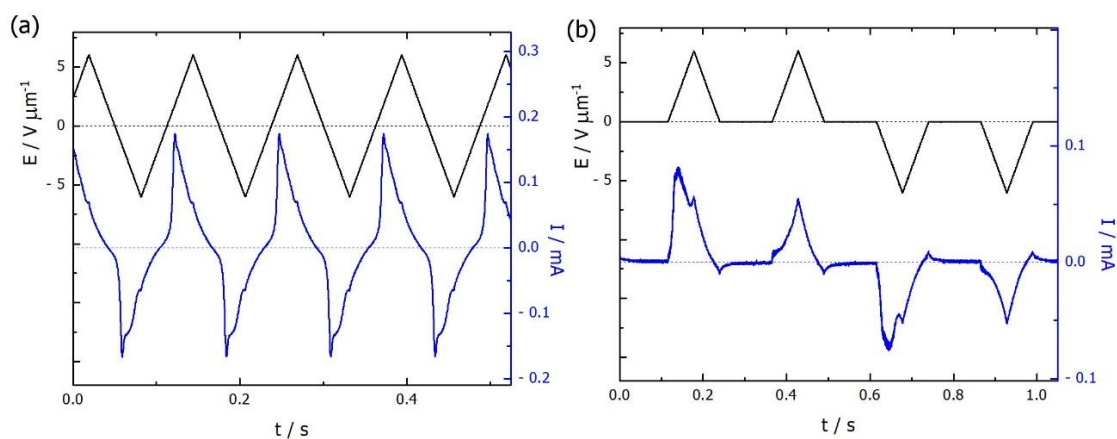


Figure S9: Switching current (blue line) recorded in  $SmC_F$  phase under application of (a) triangular and (b) modified triangular wave voltage (black line). Under application of modified triangular wave voltage the switching current peak was observed only for the first pulse of each sequence, proving stable ferroelectric ground state of  $SmC_F$  phase.

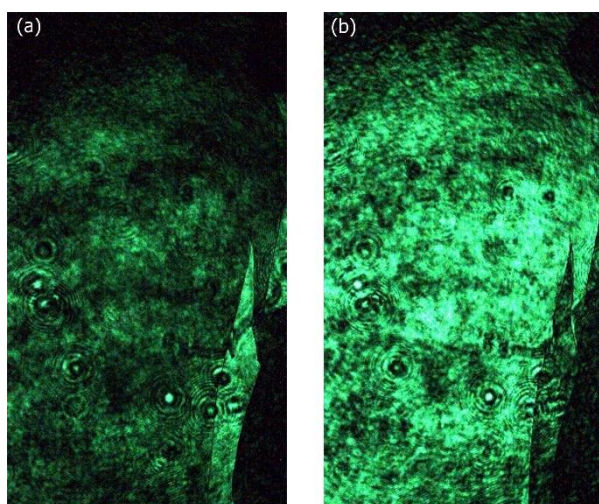


Figure S10: Images taken with SGH microscope in ground state (no applied voltage) of (a)  $SmC_F$  and (b)  $SmA_F$  phases for a sample prepared in cell with planar anchoring. Incident IR ( $\lambda=1064$  nm) radiation resulted in emission of green (SH) light in both phases, proving their ferroelectric properties.

## Supporting Information

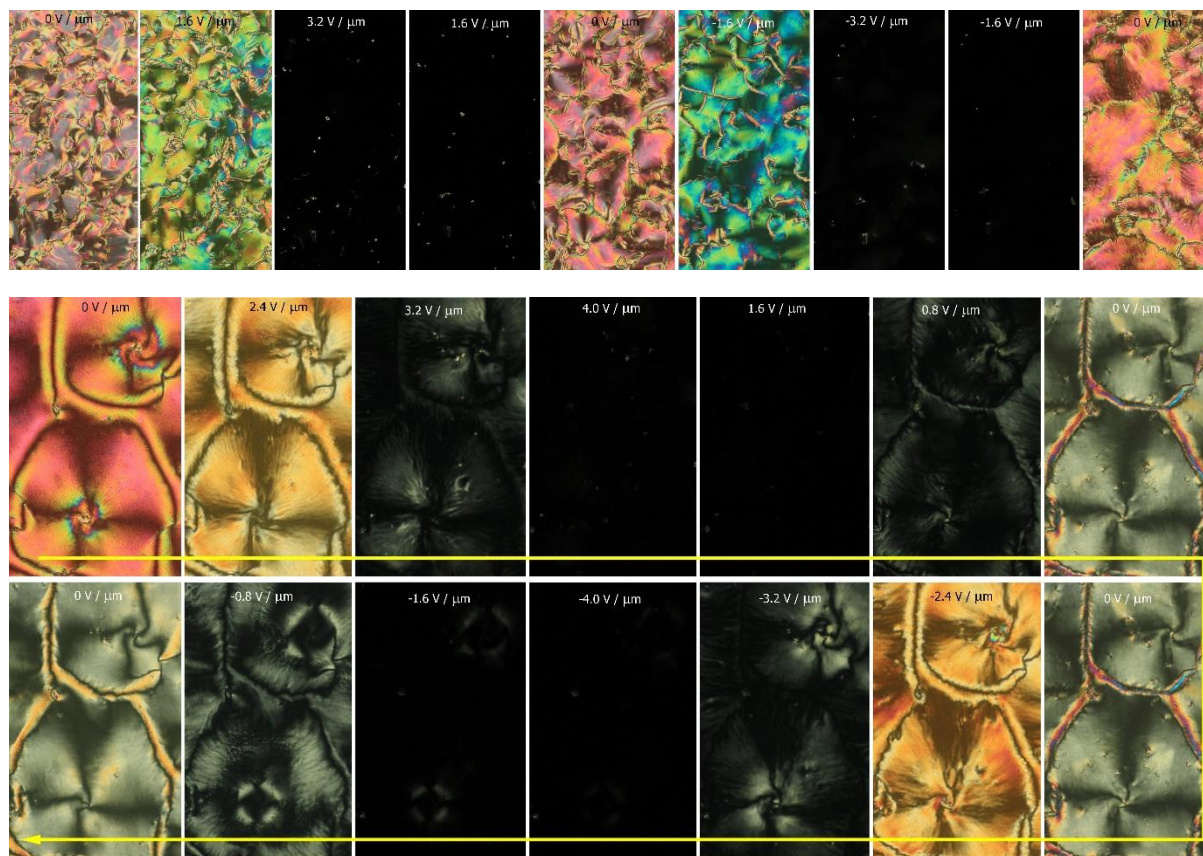


Figure S11: Optical texture changes under applied dc electric field in  $SmA_F$  (upper row) and  $SmC_F$  (bottom rows) phases. In both phases, above certain threshold voltage the homeotropic state is obtained, with polarization oriented along the applied field.

## Supplemental References

- [21] Rigaku-Oxford-Diffraction, CrysAlispro software system. Version 1.171.38.46, Rigaku Oxford Diffraction, 2019.
- [22] O. V. Dolomanov, L. J. Bourhis, R. J. Gildea, J. A. K. Howard, H. Puschmann, *J. Appl. Crystallogr.* **2009**, *42*, 339–341.
- [23] L. J. Bourhis, O. V. Dolomanov, R. J. Gildea, J. A. K. Howard, H. Puschmann, *Acta Crystallogr. Sect. Found. Adv.* **2015**, *71*, 59–75.
- [24] R. J. Mandle, S. J. Cowling, J. W. Goodby, *Chem. Eur. J.* **2017**, *23*, 14554.
- [25] J. Karcz, N. Rychłowicz, M. Czarnecka, A. Kocot, J. Herman, P. Kula, *Chem. Commun.* **2023**, *59*, 14807–14810.
- [26] A. Gavezzotti, *Acc. Chem. Res.* **1994**, *27*, 309–314.
- [27] A. Gavezzotti, G. Filippini, *J. Phys. Chem.* **1994**, *98*, 4831–4837.
- [28] C. F. Macrae, I. J. Bruno, J. A. Chisholm, P. R. Edgington, P. McCabe, E. Pidcock, L. Rodriguez-Monge, R. Taylor, J. van de Streek, P. A. Wood, *J. Appl. Crystallogr.* **2008**, *41*, 466–470.